Can Terrestrial Restoration Methodologies be Transferred to Planetary Hyperspectral Imagery? A Quantitative Intercomparison and Discussion

Shuheng Zhao ⬤, Jie Li ⬤, *Member, IEEE*, Qiangqiang Yuan ⬤, *Member, IEEE*, Huanfeng Shen ⬤, *Senior Member, IEEE*, and Liangpei Zhang ⬤, *Fellow, IEEE*

Abstract—Hyperspectral imaging is a significant remote sensing technology for deep space exploration to understand the planetary geological evolution. However, hyperspectral images (HSIs) usually suffer from various noises because of the complicated environment and equipment limitations, which leads to inconvenience to subsequent applications. In this work, a comprehensive and systematic investigation on planetary noise categories is summarized initially, and an intercomparison among state-of-the-art terrestrial joint spatial-spectral restoration models is performed to test their capability on planetary datasets. The Compact Reconnaissance Imaging Spectrometer for Mars and Observatoire pour la Minéralogie, l'Eau, les Glaces et l'Activité are adopted as examples. An improved nonreference quantitative evaluation method based on the high-resolution imaging science experiment imagery is proposed. The processed high-resolution classification result of Russell Dune can be used as the reference of unmixing after denoising. Then, spectral and spatial fidelity can be assessed indirectly. Experimental results emphasize that denoising approaches with modeling for non-independently and identically (non i.i.d.) noise characteristics are more suitable for planetary HSIs because of the diversity and complexity of their noises. This kind of method is flexible under practical circumstances and maintains the intrinsic information of HSIs better.

Index Terms—Compact reconnaissance imaging spectrometer for mars (CRISM), denoising, high resolution imaging science experiment (HiRISE) imagery, hyperspectral imagery (HSI), l'Eau, les glaces et l'activité (OMEGA), observatoire pour la minéralogie, remote sensing of planetary surface, spatial-spectral, spectral analysis.

Shuheng Zhao is with the State Key Laboratory of Information Engineering in Surveying, Mapping, and Remote Sensing, Wuhan University, Wuhan 430079, China (e-mail: photonmango@foxmail.com).

Jie Li is with the School of Geodesy and Geomatics, Wuhan University, Wuhan 430079, China (e-mail: aaronleecool@whu.edu.cn).

Qiangqiang Yuan is with the School of Geodesy and Geomatics and the Collaborative Innovation Center of Geospatial Technology, Wuhan University, Wuhan 430079, China (e-mail: yqiang86@gmail.com).

Huanfeng Shen is with the School of Resource and Environmental Sciences and the Collaborative Innovation Center of Geospatial Technology, Wuhan University, Wuhan 430079, China (e-mail: shenhf@whu.edu.cn).

Liangpei Zhang is with the State Key Laboratory of Information Engineering in Surveying, Mapping, and Remote Sensing and the Collaborative Innovation Center of Geospatial Technology, Wuhan University, Wuhan 430079, China (e-mail: zlp62@whu.edu.cn).

Digital Object Identifier 10.1109/JSTARS.2020.3024911

I. INTRODUCTION

REMOTE sensing represents the core means of Earth and planet observation. It acts as the stethoscope and the rock hammer of planetary researchers to explore the mysteries of the entire universe [1]. The visible and near-infrared imaging spectra acquired by remote sensing provides excellent results for the chemical composition and physical state of solid surfaces, thereby offering clues to present and past activities and environmental conditions.

As a powerful tool for obtaining spectra and analyzing land cover on a large scale, the number of hyperspectral images (HSI), such as the Moon Mineral Mapper (M^3) [2], the Observatoire pour la Minéralogie, l'Eau, les Glaces et l'Activité (OMEGA) [3], and the Compact Reconnaissance Imaging Spectrometer for Mars (CRISM), is increasing [4]. However, HSIs always suffer from different kinds of noises because of equipment limitations and environmental impact. Specifically, the low energy captured by each sensor produces shooting and thermal noises inevitably due to the narrow bandwidth and the radiation reduction factors, such as poor illuminating conditions and weak atmospheric and surface absorption. The limited sensor sensitivity, the photon effect, and the calibration error [5], [6] can also decrease the quality of the HSI. Moreover, the unpredicted extraterrestrial environment can complicate the noises. These noises not only degrade the HSI quality but also reduce the accuracy of subsequent planetary applications, such as classification, unmixing, and target detection.

In terrestrial remote sensing, the traditional strategy is used to restore every 2-D image band by band. However, the spectral correlation of the HSIs is ignored, thereby causing severe spectral distortions. To solve this problem, many researchers have developed various joint spatial–spectral denoising models to maintain spectral information while enhancing the spatial detail. These methods can be divided roughly into filter-based and regularization-based models. Filter-based methods usually use spatial or frequency domain operators to separate the noisy component from an image. For example, Othman and Qian [7] utilized a hybrid spatial–spectral derivative domain wavelet shrinkage noise reduction (HSSNR) approach to determine the best characteristics in the two domains. Maggioni *et al.* employed the nonlocal self-similarity (NSS) of multichannel images with Wiener filter to eliminate noises [8]. Although the

selection of appropriate threshold between noise and signal is challenging, these filters are simple and fast and have good generalization without the need of additional prior knowledge.

Recently, regularization-based methods have become the mainstream because of their efficiency and high flexibility [9]. Regularization-based approaches process the entire HSIs as a 2-D matrix or 3-D tensor, which can consider the spatial structure and spectral information simultaneously. Different kinds of prior models, such as total variation (TV) [10], sparsity [11], and low-rank [12], [13], are introduced as regularization terms by exploiting the internal features of HSIs fully,, thereby constraining the denoising problem. He *et al.* combined the TV model and low-rank property to obtain remarkable spatial results [14]. Aiming at characterizing of noises in real HSIs, Chen *et al.* used the nonindependent and identically distributed (non i.i.d.) Gaussian mixture model embedded in the low-rank decomposition model under the Bayesian framework (NMoG) [15]. HSIs, as natural tensors, its inside redundant information can be fully explored in algorithms in 3-D space. Xie *et al.* considered the global correlation along the spectrum and the NSS across space of multichannel images and then designed the Intrinsic Tensor Sparsity Regularization (ITSReg) for restoration [5]. Chang *et al.* offered an effective unidirectional low-rank tensor model [16], and the hyper-Laplacian prior is used to model the global spectral structure to alleviate ringing artifacts [17].

Nevertheless, the noises on planetary datasets have not received enough attention yet. Although incomplete data with removed noisy bands can still be utilized for analysis, it is possible to lose the key information, such as the diagnostic spectral characteristics, thereby affecting the reliability and accuracy of spectral analysis. One widely used method is CRISM Iterative Recognition and Removal of Unwanted Spiking (CIRRUS), which has been designed by Parente *et al.* [18] and has been integrated into ENVI by IDL [19]. CIRRUS first corrects residual atmospheric effects based on the discrete ordinate radiative transfer (DISORT) model [20] and then uses interpolation to eliminate the "bad" pixel in the spatial dimension and smoothen the dithering in the spectral domain. Meanwhile, the improved moment matching combined with the spline curve is used to remove the stripe. Albeit CIRRUS can smoothen jitters in the spectral dimension. However, the visual results in the spatial domain are not very ideal, thereby causing inconvenience to applications, such as multisource information fusion, extraterrestrial surface material distribution analysis, and the search for suitable future landing sites.

Parente *et al.* [18] divided the noises on planetary HSIs into two categories, namely, stripes and spiky noises. The stripe in [18] is described as a kind of detector column-dependent artifact. Spiky noise refers to uncorrected pixels with elevated bias or bad pixels that are distributed in the across-track and spectral dimensions. However, the noise types of planetary HSIs tend to be abundant due to the unpredictable and complex alien environment. Strong atmospheric absorptions at certain wavelengths for planets, such as Mars or Titan, and uncertainties on reflected radiance levels can result in saturation and data losses. For a specific example, CO_2 accounts for 95% of the Martian atmosphere, which contributes to strong signal absorption. Moreover, the nano-iron in the air causes multiple serious scattering and electromagnetic interferences that may lead to signal distortion [21]. Dust storms can also trigger unexcepted electromagnetic damage to the detectors, thereby causing dead pixels and exacerbating impulse noises and stripes. Most subsequent analysis techniques will suffer from degraded performance in the presence of noises. For instance, endmembers will be estimated incorrectly when unmixing, thereby leading to nonsensical abundances [22]. Albeit planetary HSIs are contaminated seriously, but their noise types are still similar to those of terrestrial images.

On this basis, we investigate the transferability of terrestrial restoration approaches on planetary datasets and evaluate the performance and information fidelity quantitatively. First, the noise types of the common planetary HSIs are summarized. Second, the CRISM and OMEGA datasets are taken as examples to test the capability and applicability of three types of advanced spatial-spectral hybrid methods, respectively. Because of the lack of extraterrestrial ground truth, the accompanying infrared image obtained by the High-resolution Imaging Science Experiment (HiRISE) is resorted to validate the results in the real experiment of CRISM, whereas the reference spectra [23] are used to analyze the variation of endmember extraction accuracy quantitatively before and after denoising in the real scene of OMEGA. Finally, based on the restoration results, we discuss the spatial characteristics of melting frost on the Russell Dune via the intercomparison in the CRISM case study and by exploring the component distribution on the south permanent cap through the experiments designed in the OMEGA case study.

The remainder of this article is organized as follows. Section II categorizes the noises on planetary HSIs and analyzes their specialness. Section III provides a brief introduction to the three types of algorithms. Section IV presents the quantitative evaluation indicators and the reason for selecting the unmixing as the evaluation method. Sections V and VI show the experimental results and analysis of CRISM and OMEGA datasets, respectively. Finally, the Section VII of this article puts forward the conclusion.

II. CATEGORIES OF NOISES ON PLANETARY HSIs

Detailed investigation of noises on planetary HSIs leads to the selection or construction of other suitable models. According to the statistical patterns of noises, we can divide them into the following categories.

A. Gaussian Noise

The probability density function of Gaussian noise obeys a Gaussian distribution. Poor lighting of the view field, high temperature due to long work, and interaction between circuit elements are its three primary causes. Compared with the Gaussian noise on terrestrial HSI, the planetary one may tend to be more severe (see Fig. 1). Additionally, the image of CRISM in Fig. 1(a) shows that other types of noise in the yellow dotted frame are tightly integrated with the Gaussian noise, thereby increasing the difficulty of denoising.
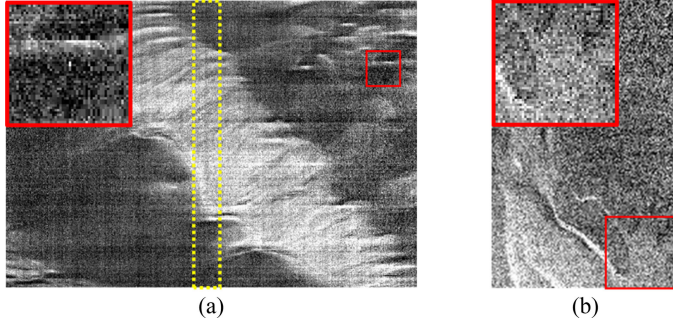
Fig. 1. Gaussian noise on prevalent planetary HSIs. (a) CRISM frt000042aa_07_if164j_ter3 Band 5 (the stripe noise is tightly bound to Gaussian noises in the yellow dotted frame). (b) OMEGA ORB0041 Band 118.
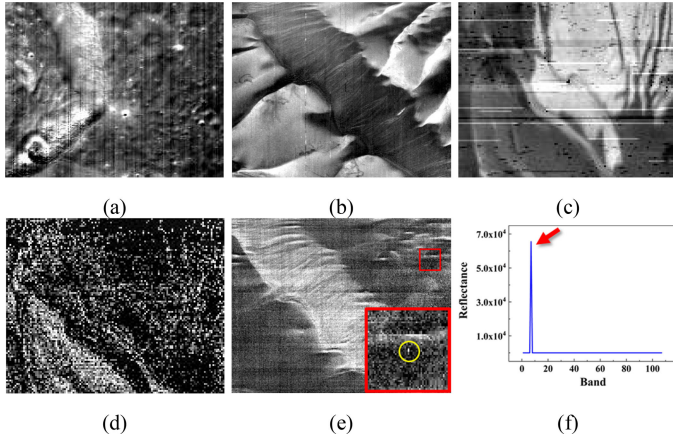

Fig. 2. Sparse noises on different planetary HSIs. (a) Stripe noise on M^3 Band 1: high-density stripes. (b) Stripe noise on CRISM frt000042aa_07_if164j_ter3 Band 361: uneven distributional and heterogeneous stripes. (c) Stripe noise on OMEGA ORB0041 Band 89: heterogeneous and multi-types of stripes. (d) Impulse noise on OMEGA ORB0041 Band 79. (e) Dead pixels on the CRISM frt000042aa_07_if164s_trr3 Band 5. (f) Spectral reflectance of dead pixel.

B. Sparse Noise

Sparse noise refers to the noise that is sparsely distributed on the image. It is mainly divided into three categories, namely, stripe, impulse noise, and dead pixels.

1) Stripe Noise: Most of the hyperspectral sensors are pushroom-type with a linear array charge coupled device. Accordingly, the stripe is the most common type of degradation in planetary remote sensing images. It occurs when the sensor responds inconsistently. Different from terrestrial images, the stripes on planetary images are heterogeneous and multidirectional, and multiple types of stripes may even exist on the same band of one dataset. Fig. 2 represents the stripe noises on different planetary images.

2) Impulse Noise: Impulse noise is also called salt and pepper noise. It can trigger large jitter in the spectral domain. Almost no serious impulse noises are found in terrestrial satellite images, but severe impulse noises exist in the widely used OMEGA images [see Fig. 2(d)]. These noises are caused by sudden electromagnetic interference.

3) Dead Pixel: Dead pixels appear when some CCD detectors breakdown or are over-saturated. Dead pixels on the

terrestrial remote sensing images are usually distributed in a linear pattern but are often displayed as dotted on planetary images. Spatial and spectral effects are shown in Figs. 2 (e) and (f), respectively. The dotted dead pixels are often easily covered by other noises and are too small to be discerned by the naked eye, thereby causing a lot of inconvenience in deep space exploration.

It can be concluded from the above investigation that planetary HSIs have more types of noise, such as impulse noise; and the degradation is more serious than terrestrial HSIs. There are two primary sources of noise: sensors and environmental factors. Assuming that the sensor manufacturing levels are the same, the main difference is caused by the environment. Therefore, we compared the main environmental factors of the Earth and Mars in Table I. For HSIs obtained mainly by the orbiters, the different atmospheric composition and land cover are the main reasons for the different sources of noise. Moreover, the dust storms that occur every year on Mars will greatly affect the data quality [40]. Meanwhile, the special land cover of Mars makes multiple reflections more serious, thereby decreasing data utilization. As for the landers and rovers, there is no magnetic field and enough atmosphere on Mars can protect them from the solar radiation; and the large diurnal amplitude will also destroy the data and the sensors themselves.

III. Joint Spatial–Spectral Restoration Methods

Mathematically, the observation model of HSIs can be expressed as

$$\mathbf{Y} = \mathbf{X} + \mathbf{N} \tag{1}$$

where $\mathbf{Y}$ is the observed HSI with mixed noise, $\mathbf{X}$ is the high-quality HSI without noise, and $\mathbf{N}$ is the noise.

To take advantage of the redundant multidimensional information, joint spatial–spectral denoising methodologies have been raised widely and have become prevalent. These methods can be divided into three categories according to the different processing principles and data expressions. Two representative methods in each category are selected for their brief introduction.

A. Filter-Based Denoising Methods

Filter-based algorithms work via analyzing and truncating specific noisy components in the spatial domain or other transformed domains. Joint spatial–spectral denoising filters mainly include two types (see Fig. 3). One performs the filtering on spatial and spectral domains at the same time and finally integrate them to obtain the final restoration results. The other one considers the image cube a 3-D block to obtain the clean results directly.

1) Hybrid Spatial-Spectral Derivative-Domain Wavelet Shrinkage Noise Reduction: HSSNR is a hybrid method of spatial–spectral wavelet shrinkage. It resorts to the dissimilarity of the signal regularity between spatial and spectral dimensions. 2-D spatial wavelet shrinkage and 1-D spectral wavelet shrinkage are used simultaneously to remove the noise in the spatial and spectral domains. Particularly, the hyperspectral data cube is transformed into the spectral derivative domain before the

TABLE I
ENVIRONMENTAL FACTORS OF THE EARTH AND MARS

|	Atmosphere	Temperature	Main Land cover	Magnetic field
Earth	■ Composition: 78% N_2, 21% O_2, and 1% noble gas. ■ Average atmospheric pressure: 101325 Pa.	■ Annual mean temperature: 288K. ■ Diurnal amplitude: lower than 50K.	■ Buildings ■ Vegetation ■ Water ■ Soil ■ Glaciers	■ Global magnetic field.
Mars	■ Composition: 95% CO_2, 3% N_2, 1.6% Ar, a little O_2, water vapor and suspended dust...... ■ Average atmospheric pressure: 600 Pa.	■ Annual mean temperature: 240K. ■ Mean diurnal amplitude: 100K.	■ Sand dunes ■ Gravel ■ Iron oxide	■ No magnetic field.
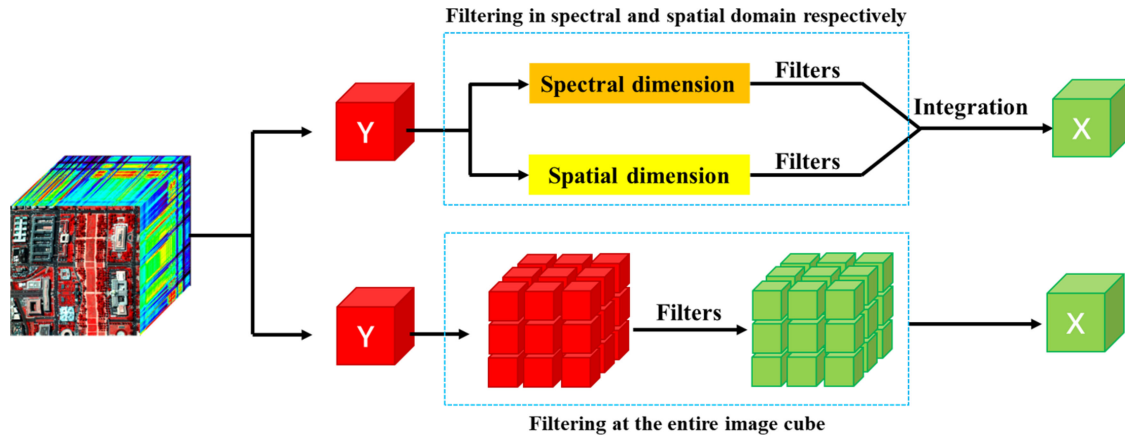
Fig. 3. Differences in workflows between two main types of filter-based denoising methods.
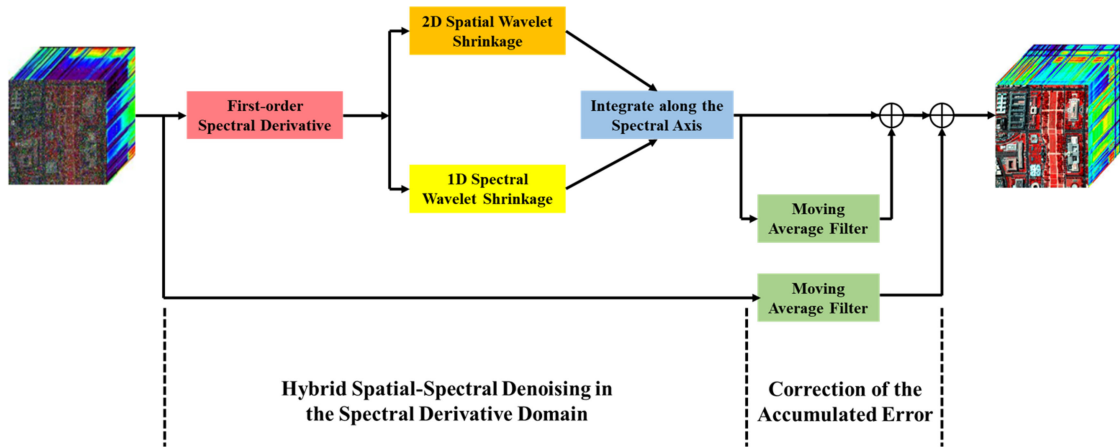

Fig. 4. Workflow of HSSNR.

wavelet shrinkage noise reduction to avoid the risk of signal deformation.

The block diagram of HSSNR is shown in Fig. 4. The HSSNR cannot only address the denoising problem of HSIs that carry low-level band-varying noise with fast operation speed but also maintains the spectral information well. However, when the noise level is high, this algorithm is not applicable anymore.

2) Block-Matching 4-D (BM4D) Filtering: BM4D is a non-local transform-domain filter based on the grouping and collaborative filtering that targets at 3-D images, such as HSIs. BM4D is mainly divided into two phases: the hard-thresholding stage and the Wiener-filtering stage. In both stages, the grouping, collaborative filtering, and aggregation steps are performed for their respective data cubes (see Fig. 5). Grouping and 4-D transform aims to find similar blocks in the whole image based on NSS and stacks them into 4-D tensors. Aggregation is utilized to obtain the final estimate by performing a weighted average of all overlapping blocks. In the hard-thresholding stages, the 4-D wavelet transform and hard-thresholding are used to reduce the noise of the 4-D tensors. In the second stage, the estimate of the first stage is regarded as the true value. It is discrete cosine transformed together with the noisy data, and then the empirical Wiener filtering is adopted to restore it.
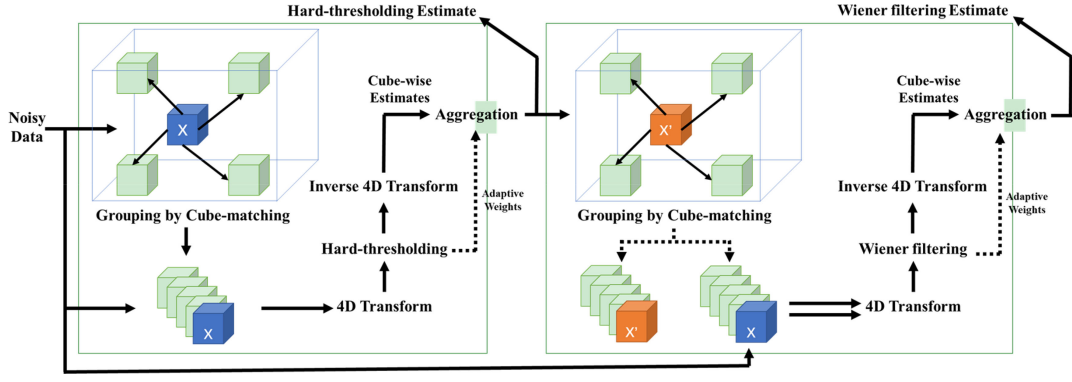
Fig. 5.　Workflow of BM4D (the blue cube is the input noisy data and the orange cube is the output of the first stage).
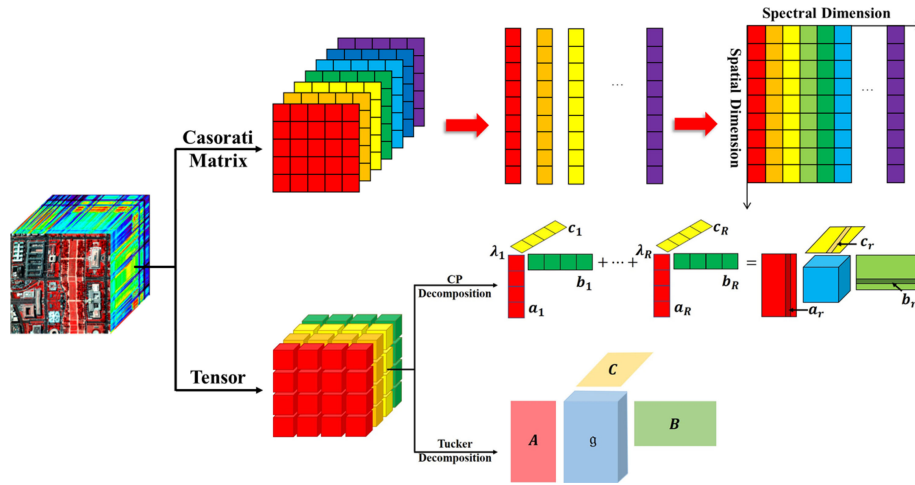

Fig. 6.　Different ways of expanding and processing the HSI cube.

B. Regularization Models With Casorati Matrix

According to the data expression, regularization models can be divided into two subtle categories. For the representation of HSI, the 2-D Casorati matrix and 3-D tensor are widely used because they consider both the spatial and spectral information. First, the Casorati matrix is introduced. Casorati matrix refers to a matrix that has columns that comprise vectorized bands of the HSI (see Fig. 6). Under the circumstance of mixed noises, the commonly used regularization priors are TV and low rank, thus two representative models will be introduced.

1) TV Regularized Low-Rank Matrix Factorization (LRTV): In low-rank matrix recovery theory, if the observed data can be expressed as the sum of a low-rank matrix and a sparse matrix, then both matrices can be obtained through optimization [24]

Fig. 7.　Graphical model of NMoG-LRMF. Yellow solid frame: estimating the low-rank matrix U. Purple dotted frame: estimating the low-rank matrix V. Red solid frame: the encoding part of noise characteristics. The blue dots: hyper-parameters. The green circle: Y_{ij} is the ith HSI element in its jth band, u_i and v_j are columns of low-rank matrix U and V, respectively. μ_j, τ_j, and d stand for the mean and variance of the mixture of Gaussians components of the jth band. z_{ij} is the hidden variable of Multinomial distribution with parameter π_j.

$$\mathbf{Y} = \mathbf{X} + \mathbf{N_S} + \mathbf{N_R} \qquad (2)$$

where $\mathbf{Y}$ is the observed HSI with mixed noises; and $\mathbf{X}$ is the clean HSI, which is low-rank. $\mathbf{Y}$ and $\mathbf{X}$ are represented as the Casorati matrix. Moreover, $\mathbf{N_S}$ is the sparse matrix that represents sparse noises, such as stripe noise and impulse noise; and $\mathbf{N_R}$ stands for Gaussian noise. LRTV provides a more detailed description of the distribution characteristics of noises.
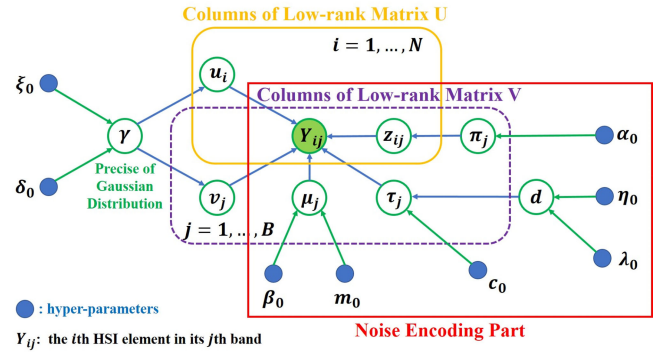
$\mathbf{N_S}$ stands for sparse noises, such as stripes, impulse noise, and dead pixels. $\mathbf{N_R}$ is the randomly distributed noise, such as Gaussian noise.

To obtain a convex optimization model, LRTV integrates the nuclear norm, TV regularization, and L1-norm in a unified-framework. The nuclear norm is used to exploit the low-rank property of the spectral domain, and the TV regularization is adopted to explore the spatial piecewise smooth structure of HSI. Meanwhile, the sparse noises, including stripes, impulse noise, and dead pixels, can be detected by the L1-norm regularization. Then, the optimization model is expressed as

$$\min_{\mathbf{X},\mathbf{S}} \quad \|\mathbf{X}\|_* + \tau\|\mathbf{X}\|_{\text{TV}} + \lambda\|\mathbf{S}\|_1$$

$$\text{s.t} \quad \|\mathbf{Y} - \mathbf{X} - \mathbf{S}\|_F^2 \le \varepsilon \operatorname{rank}(\mathbf{X}) \le r \quad (3)$$

where the anisotropic TV norm is defined as

$$\|\mathbf{X}\|_{\text{TV}} = \sum_{i=1}^{M-1}\sum_{j=1}^{N-1}\{|x_{i,j} - x_{i+1,j}| + |x_{i,j} - x_{i,j+1}|\}$$
$$+ \sum_{i=1}^{M-1}|x_{i,N} - x_{i+1,N}| + \sum_{j=1}^{N-1}|x_{M,j} - x_{M,j+1}|,$$
$$(4)$$

and the nuclear norm is

$$\|\mathbf{X}\|_* = tr(\sqrt{\mathbf{X}^T\mathbf{X}}). \quad (5)$$

2) NMoG-LRMF/NMoG: The embedded noises in HSIs are assumed as i.i.d. in most denoising algorithms, but in practice, the noises tend to be much more complex and non-i.i.d. The underestimation of statistical structures and noise complexity will reduce robustness.

NMoG models the non i.i.d. noises by utilizing the non-i.i.d. mixture of Gaussian noise assumption, which can accord well with the characteristics of noises in HSI under real scenes and adapt to various types of noises. Then, the noise modeling strategy is integrated into the low-rank matrix factorization (LRMF) model in the following equation:

$$\mathbf{X} = \mathbf{U}\mathbf{V}^T. \quad (6)$$

Moreover, the variational Bayesian algorithm is designed to derive the posterior of the model as shown in Fig. 7. The use of LRMF brings good constraints to the optimization model, and the Bayesian variational inference makes the model more adaptive and computationally efficient. Terrestrial experiments have shown that NMoG can remove various kinds of noises effectively, and the complete modeling of noise characteristics makes NMoG more robust.

C. Regularization Models With Tensor

In this section, instead of expanding the HSI into a 2-D matrix, it is treated as a 3-D tensor (see Fig. 6). Although the Casorati matrix can take advantage of the spatial–spectral correlation, the spatial structure may be destroyed because of the 2-D expansion form. As an intrinsic tensor, HSI can be processed as a 3-D data cube to maximize the correlation of information in each domain and maintain the natural properties. Similarly, two state-of-the-art models are selected for testing.

1) Intrinsic Tensor Sparsity Regularization: In this method, two intrinsic features that contain the global correlation along spectrum and the NSS across space are fully considered to constrain the solution. Moreover, intrinsic tensor sparsity (ITS) measure is used to measure the sparseness of the tensor.

In ITSReg's workflow, self-similar blocks are expanded and stacked to a new tensor. Then, the new tensor is applied to the ITS prior its optimization for denoising. The optimization problem of ITSReg is

$$\mathbf{X}_i = \arg\min_{\mathbf{X}} \mathrm{S}(\mathbf{X}) + \frac{\gamma}{2}\|\mathbf{Y}_i - \mathbf{X}\|_F^2 \quad (7)$$

$\mathrm{S}(\mathbf{X})$ is the sparsity measure of a tensor $\mathbf{X}$

$$\mathrm{S}(\mathbf{X}) = t\|\mathbf{S}\|_0 + (1-t)\prod_{i=1}^{N}\operatorname{rank}(\mathbf{X}_i) \quad (8)$$

where $\mathbf{S}$ is the core tensor of $\mathbf{X}$ obtained from the Tucker decomposition.

This algorithm works well at removing noise on multichannel images but relies heavily on memory. Consequently, large-sized data can make the model relatively memory intensive and time consuming.

2) Hyper-Laplacian Regularized Unidirectional Low-Rank Tensor Recovery (LLRT): Unfortunately, ITSReg ignores the difference of the natural structure correlation under the NSS, spatial sparsity, and spectral correlation modes. Therefore, the NSS is selected to be the key ingredient in LLRT after analyzing the rank properties in 2-D and 3-D cases.

The NSS is adopted to explore self-similar subcubes. After unfolding them into a new tensor, a unidirectional low-rank regularization term is applied to it. Moreover, the hyper-Laplacian prior is utilized to model the global spectral structure, which alleviates the ringing artifacts in the spatial dimension indirectly. Incorporating all the priors, the model becomes

$$\left\{\hat{\mathbf{X}}, \hat{\mathbf{L}}\right\} = \arg\min_{\mathbf{X},\mathbf{L}_i} \frac{1}{2}\|\mathbf{X} - \mathbf{Y}\|_F^2 + \mu\|\nabla_Z\mathbf{X}\|_p$$
$$+ \omega\sum_i\left(\frac{1}{\lambda_i^2}\|R_i\mathbf{X} - \mathbf{L}_i\|_F^2 + \operatorname{rank}_2(\mathbf{L}_i)\right) \quad (9)$$

where $\mathbf{X}$ is the noisy nonlocal block, while L is the clean nonlocal block. $\mathbf{R}_i\mathbf{X}$ represents the constructed tensor for each exemplar cubic, and p $(0 \le \mathrm{p} \le 1)$ is the parameter to control the sparsity of hyper-Laplacian. While $\operatorname{rank}_2(\mathbf{L}_i)$ is used to constraint the unidirectional low-rank property of the solution. The design of multiple regularization parameters can balance the correlation of different constraints in various domains.

IV. RESTORATION PERFORMANCE QUANTITATIVE EVALUATION INDICATORS

To evaluate the effectiveness of these methods, quantitative indicators are used indispensably to assess the quality of the denoising image. Owing to the 2-D spatial and 1-D spectral information that exists in the HSI, the spatial restoration results and the degree of spectral distortion must be assessed simultaneously. Two spatial indicators and four spectral measures will

be introduced in the next subsections. Spatial evaluation indices of HSI denoising.

The denoising results in the spatial domain can be assessed subjectively through the perception of the observers, which varies from person to person or can be conducted objectively by using quantitative indicators; the latter is more convincing. The two widely used indicators are introduced as follows:

Mean Peak Signal to Noise Ratio (MPSNR):

$$
\begin{aligned}
\text{MPSNR} &= \frac{1}{B} \sum_{k=1}^{B} \text{PSNR}_k \\
&= \frac{1}{B} \sum_{k=1}^{B} 10 \lg \frac{A^2}{\frac{1}{MN} \sum_{i=1}^{M} \sum_{j=1}^{N} (x(i,j,k) - y(i,j,k))^2}
\end{aligned}
\tag{10}
$$

where M, N, and B are the width, height, and bands of the HSI, respectively; A is the maximum value of all the image gray values; $x(i,j,k)$ is the denoised image; and $y(i,j,k)$ stands for the original input image. The higher the MPSNR is, the better denoising result is.

Mean Structural Similarity Index (MSSIM):

$$
\text{SSIM} = \frac{(2\mu_x \mu_y + C_1)(2\sigma_{xy} + C_2)}{(\mu_x^2 + \mu_y^2 + C_1)(\sigma_x^2 + \sigma_y^2 + C_2)}
\tag{11}
$$

where μ_x and μ_y stand for the mean values of the denoised and original images, respectively; σ_x^2 and σ_y^2 are the variances; σ_{xy} is the covariance; C_1 and C_2 are constants that prevent the denominator from being 0. The mean value of SSIM of each band is employed to assess the whole structural similarity, the closer MSSIM is to 1, the better the result is

$$
\text{MSSIM} = \frac{1}{B} \sum_{i=1}^{B} \text{SSIM}_i.
\tag{12}
$$

A. Spectral Evaluation Indices of HSI Denoising

Mean spectral angle mapper (MSAM):

$$
\text{MSAM} = \frac{1}{MN} \cos^{-1} \left[\frac{\sum_{i=1}^{MN} t_i r_i}{\sqrt{\left(\sum_{i=1}^{MN} t_i^2\right)\left(\sum_{i=1}^{MN} r_i^2\right)}} \right]
\tag{13}
$$

where t_i represents the denoised spectrum of the ith pixel, and r_i stands for the original one. It can assess the spectral fidelity after denoising. The lower MSAM is, the more similar the two spectra will be.

Aside from the classification, the unmixing can also be chosen to evaluate the denoising algorithms further. On the one hand, the intercomparison of the extracted endmember is a direct way to check spectral fidelity. On the other hand, the abundance map can illustrate the restoration results of spatial and spectral dimensions simultaneously. Therefore, three indexes that correspond to the HSI unmixing are introduced as the spectral indicators in this article.

Spectral Information Divergence (SID):

$$
\text{SID} = \text{D}(a|\hat{a}) + \text{D}(\hat{a}|a)
\tag{14}
$$

where a is the true endmember signature, $\hat{a}$ is the estimated one, and D is the asymmetrical relative entropy:

$$
\text{D}(a|\hat{a}) = \sum_j p_j \lg \left(\frac{p_j}{\hat{p}_j} \right)
\tag{15}
$$

where p is the probability distribution vector with each endmember spectrum

$$
p = \frac{a}{\sum_j a_j}.
\tag{16}
$$

The spectral information divergence is a kind of information-theoretic measure. It is used to describe the variability of the spectra.

Abundance Angle Distance (AAD) and Abundance Information Divergence (AID):

$$
\text{AAD} = \cos^{-1} \frac{s^{\text{T}} \hat{s}}{\|s\| \|\hat{s}\|}
\tag{17}
$$

$$
\text{AID} = \text{D}(s|\hat{s}) + \text{D}(\hat{s}|s)
\tag{18}
$$

where s represents the abundance vector of a ground truth pixel, and $\hat{s}$ is the estimated one. As for the estimation of the abundance map, the AAD and AID are employed to measure the results by substituting the extracted spectra with the abundance vector of every pixel. As shown in the aforementioned formulas, the lower the four indicators are, the closer they are to the ground truth.

Combining multiple indicators can fully explore recovery accuracy and validate the subsequent unmixing results.

V. CRISM CASE STUDY

Simulated and real experiments are carried out on the basis of real images, and the corresponding high-resolution image is used to assess the results of real experiments in this case study quantitatively. The spatial distribution of melting frost on the Russell Dune and the causes are analyzed according to the denoising results.

VI. CRISM CASE STUDY

Simulated and real experiments are carried out on the basis of real images, and the corresponding high-resolution image is used to assess the results of real experiments in this case study quantitatively. The spatial distribution of melting frost on the Russell Dune and the causes are analyzed according to the denoising results.

A. CRISM Dataset

CRISM is the visible infrared spectrometer on the Mars Reconnaissance Orbiter (MRO) and is used to search for mineralogical indicators of past and present water on Mars [4]. CRISM's spectrometer has two detectors: S detector has 107 visible and infrared bands (370–1100 nm) and L detector has 437 infrared bands (1000–3920 nm). Under the target mode, CRISM is imaged in 544 bands with the spectral resolution of

TABLE II
QUANTITATIVE EVALUATION OF THE DIFFERENT DENOISING ALGORITHMS WITH THE SIMULATED DATA

Index	Noisy	CIRRUS	HSSNR	BM4D	LRTV	NMoG	ITSReg	LLRT
MPSNR	22.3214	22.3214	28.1270	33.8134	35.8660	**36.8782**	34.0683	33.9561
MSSIM	0.5018	0.5018	0.7471	0.9250	0.9462	**0.9515**	0.9415	0.9353
MSAM	11.2268	11.2268	6.3408	3.1372	3.8366	2.7294	2.9743	**2.6777**
SID	34.7480	26.5759	0.0006	0.0094	**0.0005**	0.0010	0.0015	0.0094
AAD	66.5104	68.0155	57.2536	60.8791	57.7231	**46.9828**	59.7098	59.5054
AID	18.6414	17.6683	9.3082	6.2745	**4.5468**	5.4396	12.4650	14.8373
Time/s	/	38.6574s	**24.6278**	458.5296	279.1247	245.8408	1008.7463	530.1746

6.55 nm, and the spatial resolution is 15–19 m. The excellent resolutions make CRISM play an important role in studying the distribution of water-bearing minerals, carbon dioxide, and solid water cycles and cannot eliminate the stripes on Mars.

B. Study Area

Russell crater is situated in Noachis quadrangle, 54.9 ° south latitude and 347.6 ° west longitude, its diameter is approximately 135 km. The main research area is the Dune on the crater. Some gullies are found on the Dune which are a little different from gullies in other places, like the walls of craters. A striking feature is that the gullies on Russell Dune seem to maintain the same width for a long distance and usually end with a pit instead of an apron [25].

At the end of winter on Mars, white frost and gullies have distinct differences in terms of brightness and imaging spectra, thereby making their separation in high-resolution images and HSIs easy. Therefore, the high-resolution data of this special area can be used as the reference to evaluate the degree of spectral distortion before and after denoising quantitatively.

C. Simulated Experiment

Particularly, clean bands extracted from CRISM frt000042 aa_07_if164s_ter3 are used to produce a $200 \times 200 \times 132$ cube, in which controlled sources of noise are added. In the simulated experiment, non-i.i.d. Gaussian noise is added to all the bands. The SNR varies from 10 to 25 dB randomly. Stripes are added to four bands from band 11 to band 14. The width of stripes is 2 to 3 lines. Dead pixels are simulated for bands 21 and 31 in the size of 2×2. Impulse noise is added to 11 selected bands from band 41 to band 51.

Minimum volume constrained non-negative matrix factorization (MVC-NMF) [26] is used to perform unmixing to the HSIs before and after denoising. MVC-MNF decomposes highly mixed pixels of HSI based on non-negative matrix factorization and minimum volume constraints without pure pixel assumption, and it has already proved to be effective on simulated and real datasets, especially experiments in [26] indicate that MVC-NMF has the potential to identify these less prevalent endmembers, which are more favorable for extracting alien endmembers. The parameters are set in accordance with Ceamanos's research [27].

All experiments are conducted using MATLAB R2019b on a PC equipped with eight Intel Xeon E5-2620 CPU (at 2.10 GHz) and 16-GB RAM.

Fig. 9 shows the denoising results of the different algorithms, and Table II gives the quantitative evaluation index of the restoration results. The bolder indexes are the best, and the underlined indexes follow. The visual effects suggest that CIRRUS can neither remove the non-i.i.d. Gaussian noise and dead pixels nor eliminate the stripes very well. Therefore, this method does not work when the mixed noise is complicated and serious. Combining the visual results and six indicators, it concludes that the regularization models with Casorati matrix performs best, but NMoG works better and faster than LRTV according to the quantitative indicators in Table II. Fully exploiting the correlation between spatial and spectral domains and considering the features of noises allows it to remove mixed noises effectively. In contrast, tensor-based models work moderately, because they are limited in the design of noise characteristics. As for the filer-based methods, HSSNR shows its great spectral fidelity while BM4D shows better spatial recovery ability, but HSSNR cannot remove sparse noises.

D. Real Experiment

In real experiment, the CRISM frt000042aa_07_if164s_ter3 is still used. Considering the illumination variability due to the topography of the research area, we finally opt for the 3 km $\times$ 3 km area with the size of 180 pixel $\times$ 180 pixel, which focuses on gullies and frost as the region of interest. Given that light in the visible channels is susceptible to strong scattering by iron oxide aerosols present in the atmosphere, only bands in the range of 1.0–2.6 μm are selected. The size of the real image is 180 $\times$ 180 $\times$ 242.

1) Improved Validation Method for Real Experiments: The quantitative assessment of denoising results cannot be done directly because of the lack of ground truth. To solve this problem, an improved HiRISE-based validation approach is proposed.

Generating the Reference Map: HiRISE is a camera onboard the MRO that consists of a 0.5 m aperture reflecting telescope. It can take pictures of Mars with resolutions up to 0.25 m and can be used to view more details on the surface of Mars [28]. HiRISE can obtain three-channel pictures at blue-green, red, and near-infrared wavelengths, whereas the red-channel image has five times the width of the others, thereby covering our whole study area. Therefore, the red-channel image is utilized in our
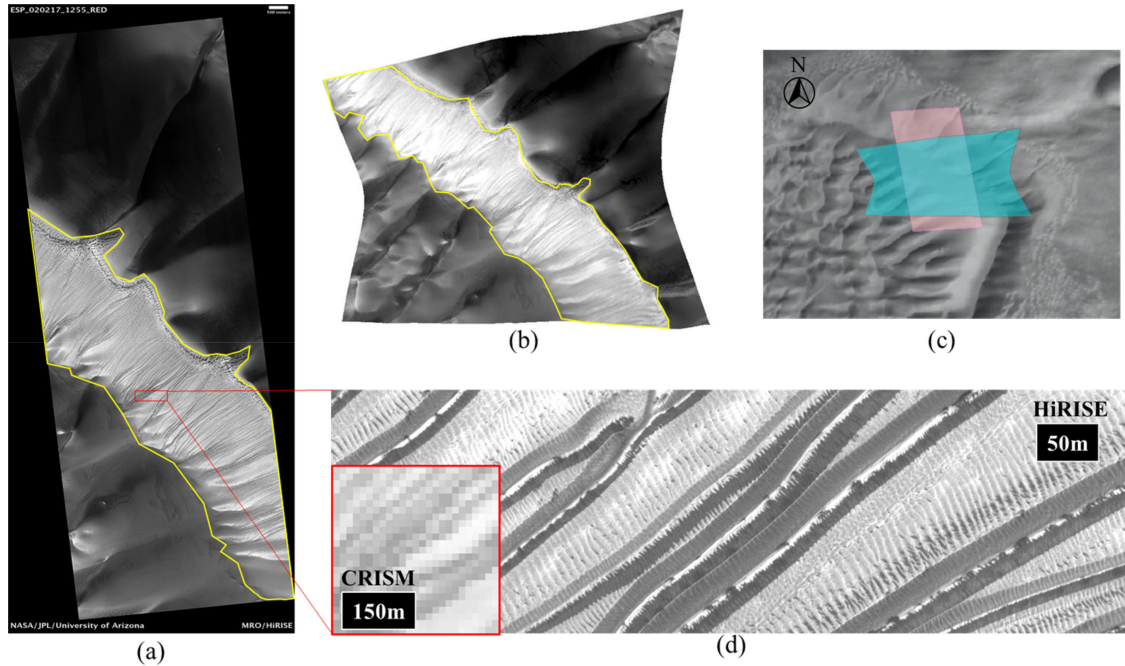
Fig. 8. Russell Dune in CRISM and HiRISE, and the range surrounded by the yellow line is our region of interest (ROI). (a) HiRISE ESP_020217_1255_RED. (b) CRISM frt000042aa_07_if164s_ter3 Band 123 (map projected). (c) Location of the test images over the mega Dune on the THEMIS Day IR Global Mosaic (Pink: HiRISE; Cyan: CRISM). (d) Details of the gullies on the Russell Dune, the dark strip line features are regarded as gullies.

experiment. HiRISE and CRISM are onboard the same orbiter, which means they can capture images from the same area simultaneously. The footprints of the CRISM image FRT000042aa and HiRISE image PSP_002482_1255 are shown in Fig. 8.

Significantly, the resolution of CRISM will decrease after projection, and thus denoising is conducted before it. Meanwhile, unmixing the denoising results before projection and registration is unreliable because the geometric errors will cause the loss of details on the abundance map. Therefore, restoration is carried out before projection while unmixing is executed after projection and registration.

ISODATA Classification: According to the geomorphology analysis and the grayscale histogram, the HiRISE image is divided into two categories, namely, bright frost and dark features (gullies). Iterative self-organizing data analysis techniques algorithm (ISODATA) [29] is adopted because it has the flexibility to determine the number of clusters automatically, which is suitable for the extraterrestrial environment without prior knowledge. The HiRISE image is divided into seven categories via ISODATA. The category with the lowest average gray level is selected after excluding the pixels of shadow by local thresholding. Only dark and elongated features are classified as dark features, the rest is classified as bright frost.

Downsampling: After classification (dark features: 1, bright frost: 0), the results (average of 72×72-pixel classification results which consist of 1 and 0) were downsampled by 72 times (the results are between 0 and 1), and then the reference abundance map of the dark features can be obtained.

Registration: Initially, the edge detection is used to extract the edges of two images. Afterward, the Fourier-Mellin transform [30] is applied to coarse registrate. Then, the Harris corner

extraction [31] is performed on the reference image, and random sample consensus (RANSAC) [32] operator is used to exclude error points for fine registration. The whole root mean square error (RMSE) is 0.5833 pixel, the mean local correlation coefficient and the global correlation coefficient with 0.9892 and 0.9570 are accurate enough for the following operations. The workflow of the registration part is illustrated in Fig. 10.

2) Unmixing Performance on the Denoised Martian Data: The spatial results are basically consistent with the simulated experiments (see Fig. 11). CIRRUS is not effective for serious Gaussian and sparse noises. As for the filter-based methods, HSSNR cannot remove most of the noises because its model cannot handle non-i.i.d. noises. On the contrary, BM4D can reduce most of the noises, but oversmoothing exists, and dead pixels cannot be removed completely. Regularization models have achieved good overall visual results, but matrix-based variational models cannot remove inapparent stripes that are too close to the texture of the image itself, whereas tensor-based can remove them at the expense of over smoothing.

The endmembers extracted by MVC-NMF are shown in Fig. 12. Based on the reference abundance map, the endmembers, which are supposed to be dark features but separated due to nonhomogeneous illumination conditions, are selected by Pearson correlation coefficient r and visual check, and then merged into the entire abundance map in Fig. 13. In Table III, the first row means the selected endmembers as dark features, and r and RMSE show the proximity to the reference map. Combining the quantitative indicators and the abundance maps, we find that CIRRUS's unmixing result is unreliable because it loses key spatial structure. Regularization models based on matrix still perform best, especially for NMoG and LLRT, which have
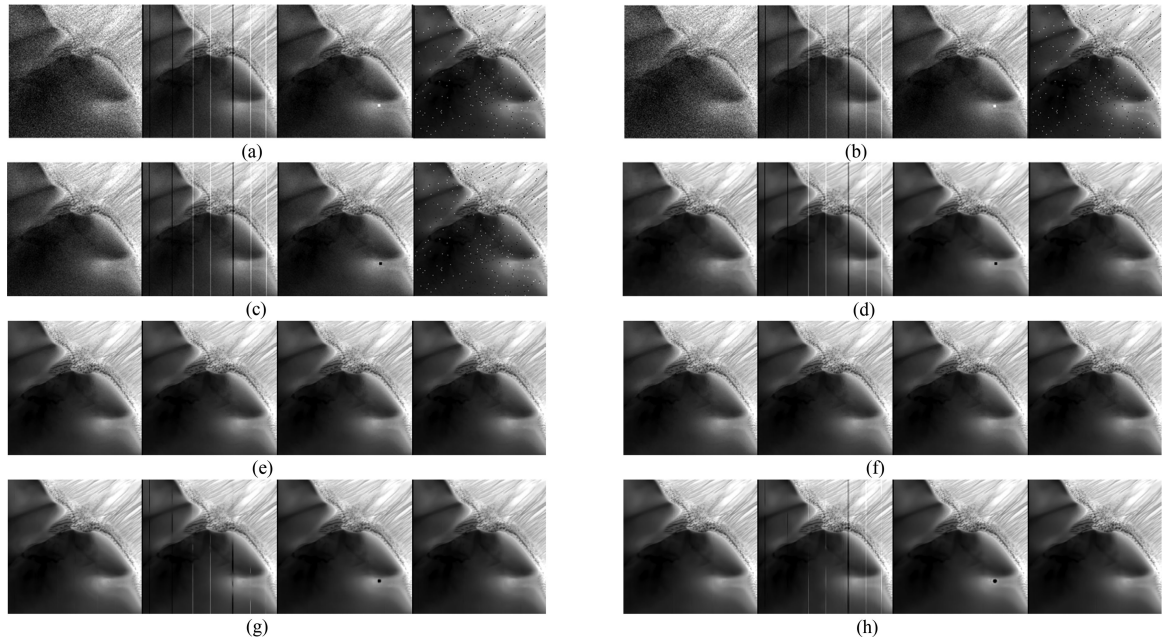
Fig. 9.   Restoration results in the simulated experiment. (a) Noisy. (b) CIRRUS. (c) HSSNR. (d) BM4D. (e) LRTV. (f) NMoG. (g) ITSReg. (h) LLRT
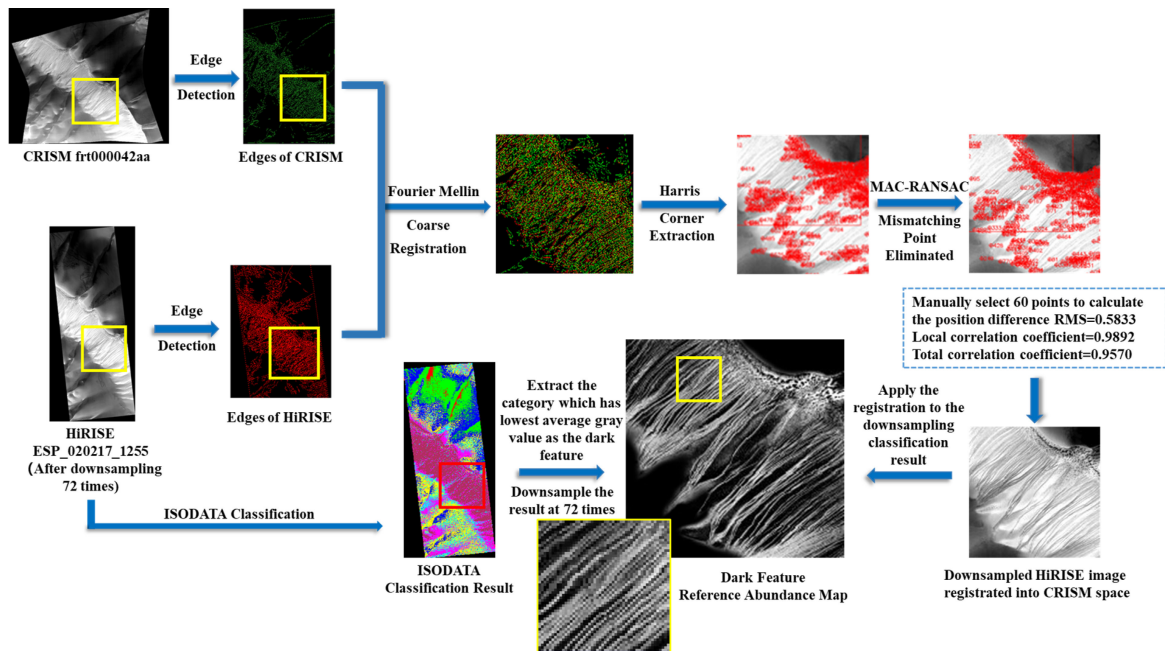

Fig. 10.   Workflow of generating the dark feature reference abundance map.

the most accurate abundances owing to the smallest spectral distortion. Given the more obvious oversmoothing presented on the results of tensor-based models, the estimated abundances are closer to the reference map in a large range.

E. Characteristic Activity on Denoising Russell Dune Case

1) Fidelity in Both Spatial and Spectral Dimensions: Fig. 14 shows the endmember signatures of NMoG that obtains the best denoising result. According to Gardin *et al.* [33], the spectral

signatures are consistent with the CO_2 ice spectral signature mixed with a small amount of water ice. All the spectral curves have nearly the same diagnostic spectral features and shapes. The spectra show absorption bands diagnostic of CO_2 ice at 1435 nm and a weak but obvious absorption band diagnostic of water ice at 1500 nm.

Previous research [34], [35] proved that reflectance and emissivity changes in the seasonal ice cap mainly depended on the compositions (e.g., the content ratio of CO_2 ice to water ice), grain sizes, the dust content, and the porosity. However, these
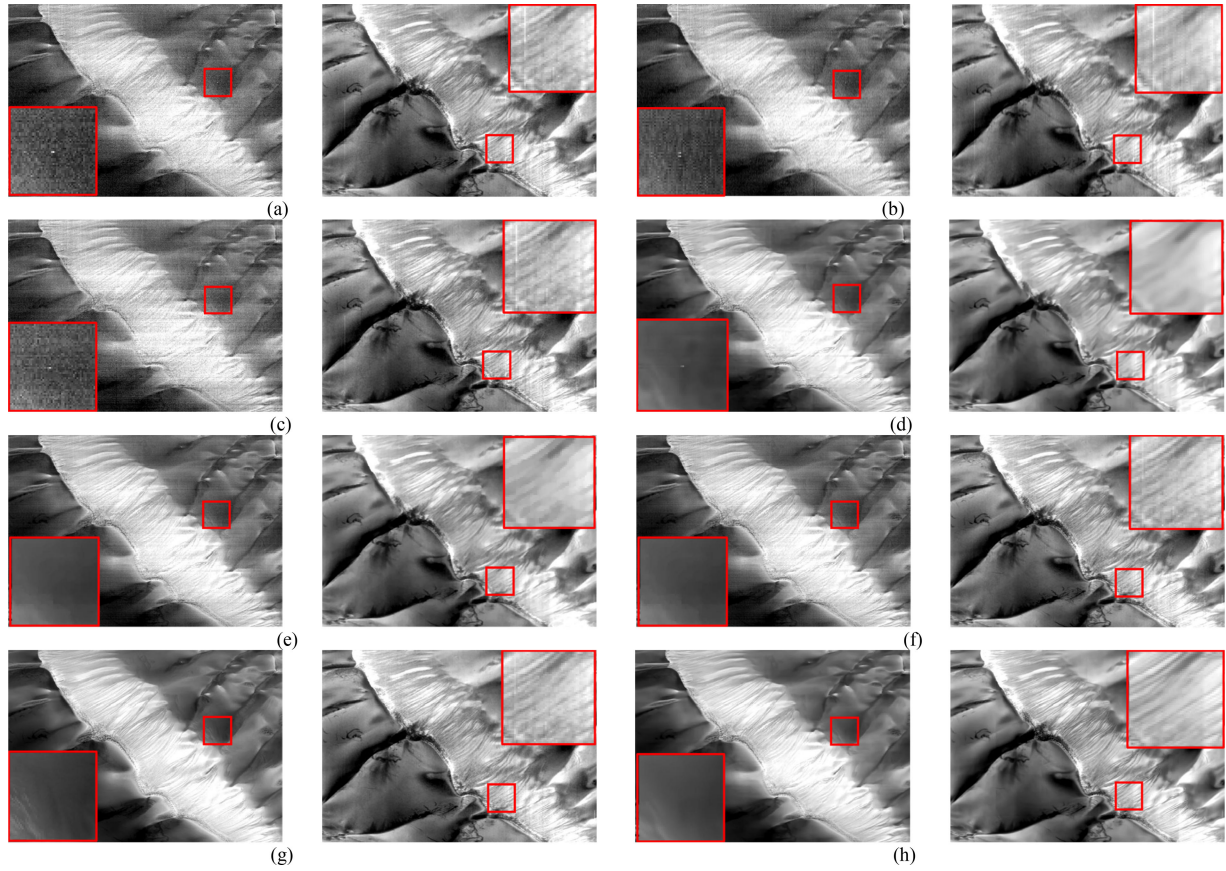
Fig. 11.   Restoration results in real experiment. (a) Original: left: 1042.90 nm right: 2027.03 nm. (b) CIRRUS. (c) HSSNR. (d) BM4D. (e) LRTV. (f) NMoG. (g) ITSReg. (h) LLRT.
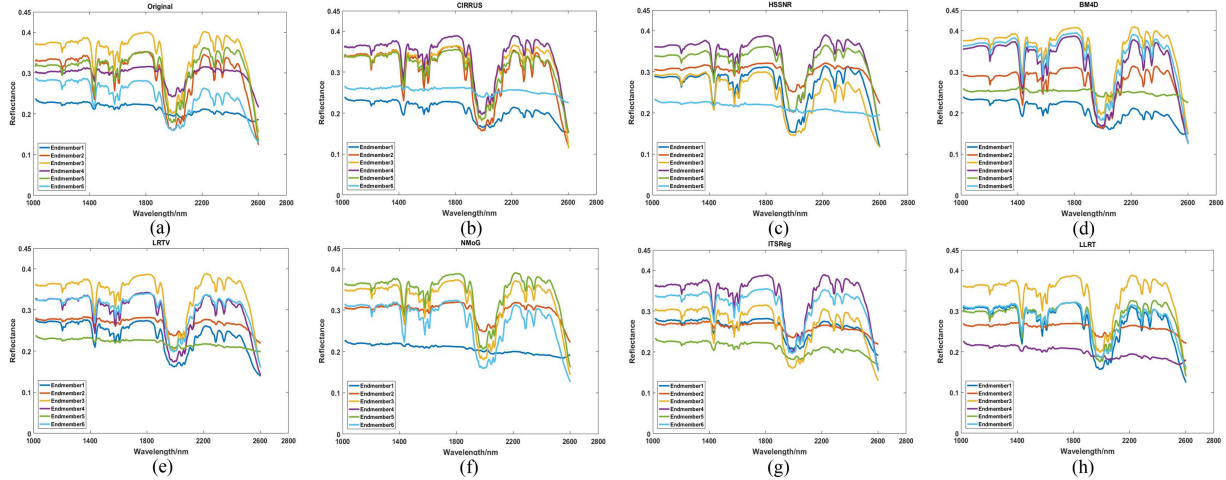

Fig. 12.   Spectral signatures of extracted endmembers. (a) Original. (b) CIRRUS. (c) HSSNR. (d) BM4D. (e) LRTV. (f) NMoG. (g) ITSReg. (h) LLRT.

studies only focused on the changes in different solar longitudes but did not consider the changes in the same location. On the foundation of the above study and the endmember extraction results after denoising, we can find that joint spectral–spatial denoising methods can extract the correct endmembers and preserve the differences among them. Especially, only one endmember with the lowest reflectance of NMoG is selected as a dark feature, showing that better unmixing results can be obtained

after denoising. Importantly, by analyzing the results of Russell Dunes and the phenomenon that the same spectral signatures have different reflectance, the spatial distribution characteristics of frost melting at the end of winter can be obtained. First, the degree of ice cover melt varies from location to location. Furthermore, different locations have frost with different CO_2 ice to water ice content ratios concerning the depth of the absorption features. Finally, frost in different locations has varying
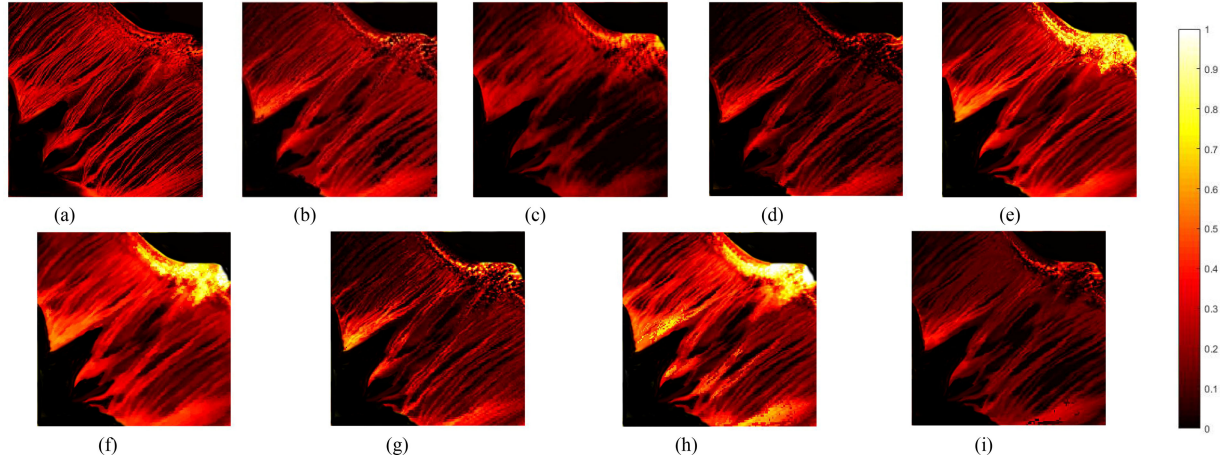
Fig. 13. Abundance maps of the dark features. (a) Reference. (b) Original. (c) CIRRUS. (d) HSSNR. (e) BM4D. (f) LRTV. (g) NMoG. (h) ITSReg (i) LLRT

TABLE III
QUANTITATIVE INDICATORS OF THE UNMIXING RESULTS

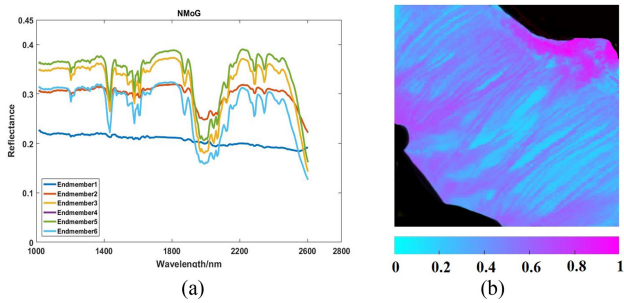| Index	Original	CIRRUS	HSSNR	BM4D	LRTV	NMoG	ITSReg	LLRT
Endmember	1,4,6	1,6	1,3,6	1,2,5	1,2,5	1	1,2,5	2,4
r	0.6111	0.7313	0.8169	0.8867	0.8748	**0.8956**	0.8694	<u>0.8928</u>
AAD	63.1802	71.3758	61.8536	<u>60.8791</u>	66.7082	**59.3572**	64.8048	63.4233
AID	6.9457	17.6683	**5.4238**	8.1232	10.4252	<u>6.7429</u>	8.4325	7.4284

Fig. 14. Same spectral shape with different reflectance and the distributions of melting frost after denoising. (a) Endmembers of NMoG. (b) Distribution of melting degree.

Fig. 15. Comparison of the highest reflectance endmember.
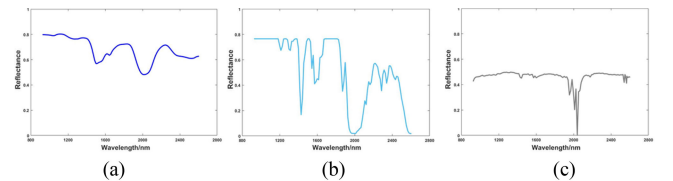
Fig. 16. Reference spectral signatures of three typical Mars components simulated by numerical models. (a) Water ice. (b) CO_2 ice. (c) Dust.

properties, such as grain size, the dust content, and porosity. From the perspective of the degree of melting, the endmember with the lowest reflectance has the greatest melting degree. The melting degree of the Russell Dune can be mapped by dividing the melting degree into six levels. This distribution of melting degree is consistent with the spatial distribution of the gullies and frost on the optical image.

2) Facilitation to Atmospheric Correction: To further explore the change in spectral fidelity, the endmember with the highest reflectance in each method is regarded as the same endmember and is chosen to be compared in Fig. 15. Most of the denoising signatures have nearly the same reflectance with each other but lower than the original noisy curves.

Because the atmosphere has an obscuring effect on bright ices, the reflectance of bright ices usually rises after the atmospheric

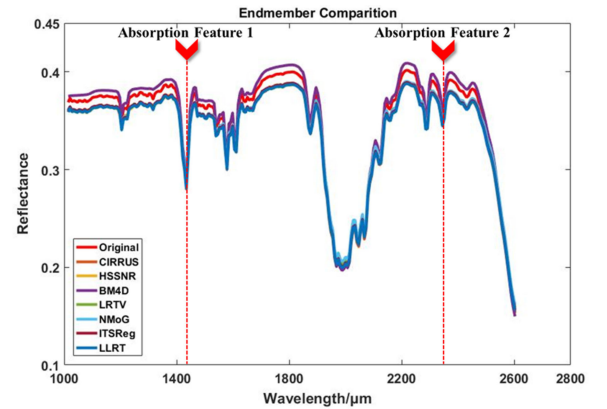correction. However, the covering on the Russell Dune is a mixture of CO_2 ice and water ice with the reflectance less than 0.4, which does not match the feature of bright ices, hence the speculation that the drop of reflectance after denoising results
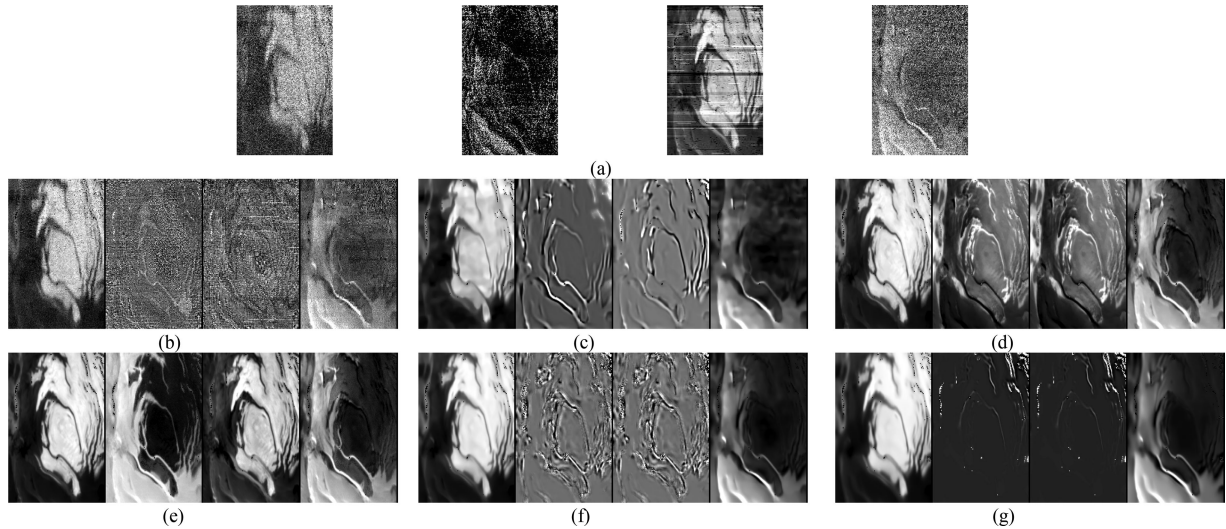
Fig. 17. Denoising results of OMEGA case study. (a) Original: Band 1: Gaussian noise; Band 79: Impulse noise; Band 89: Stripes; Band 118: Gaussian Noise (more serious). (b) HSSNR. (c) BM4D. (d) LRTV. (e) NMoG. (f) ITSReg. (g) LLRT.

from the further atmospheric correction is reasonable. Meanwhile, as mentioned in Section I, a further and more accurate atmospheric correction mode DISORT is involved in CIRRUS. Except for BM4D, the reflectance of all the joint spatial–spectral denoising methods are consistent with CIRRUS. Therefore, we infer that these restoration algorithms can affect the atmospheric correction of planetary HSIs positively.

VII. OMEGA CASE STUDY

OMEGA is a widely used Martian hyperspectral dataset. Compared with CRISM, OMEGA has a wider range of wavelength, but its noises are more complex and serious. In this case study, instead of using auxiliary high-resolution images as the reference, the reference spectra simulated by a surface reflectance model [36] is applied for denoising validation. Therefore, the quantitative intercomparison among algorithms on the OMEGA case can be achieved by contrasting the accuracy of endmember extraction before and after denoising.

A. OMEGA Dataset and Study Area

OMEGA is a high-resolution visible and infrared imaging spectrometer on the Mars express launched by the European Space Agency in 2003. Its main mission is to detect the composition of rocks, minerals, and ice on the surface of Mars, as well as the composition of the Martian atmosphere. The instrument is composed of visible channels and near-infrared and infrared channels, and its spectrum covers the range of 360–5100 nm with a total of 352 bands. Given that the Mars Express has an elliptical orbit, OMEGA's spatial resolution varies, ranging from 0.3 to 4.8 km. In recent years, the OMEGA dataset has explained the diversity and complexity of mineral composition on the Martian surface successfully and has been verified by the field test and analysis of the spirit and the opportunity landers and the thermal emission spectrometer inversion results [37]. However, due to internal and external factors, the OMEGA images also undergo various kinds of noises. In the experiments, OMEGA HSI ORB0041 [38] with the size of 128×200 and contains the south polar permanent cap and layered deposits of Mars is used to analyze restoration performance.

B. Experiments and Analysis

For the same reason clarified in Section V, only bands 1–125, which covers from 926 to 2605 nm, are selected. The image has already been preatmospherically corrected preliminarily.

Three major surface chemicals, namely, water ice, CO_2 ice, and mineral dust, have been surely detected in this area [38]. Fig. 16 shows the reference spectra of three typical Martian components calculated by using numerical modeling [36].

According to [23], the number of endmembers is set as 5. The restoration results are shown in Fig. 17. Fig. 18 represents the endmembers extracted from the original and denoising images. Fig. 19 shows the abundance maps of three components. r and MSAM before and after denoising are presented in Table IV. MVC-NMF may extract spectra that do not exist in the HSI, and the abundance values of these nonexistent endmembers are usually so low that they can be ignored. Hence, we choose and exhibit endmembers that have higher values of r than the three components.

1) Endmember Analysis on the Denoising OMEGA Data: The accuracy of endmember extraction is improved after denoising via visual results. NMoG still achieves the best result, but LRTV shows larger spectral distortion in agreement with the results in the CRISM case study. Although filter-based methods and tensor-based models can remove Gaussian noise, they are inapplicable to other noises.

The accuracy of the endmember extraction has increased after filters and Casorati matrix-based regularization models have been applied. However, the tensor-based methods cannot extract the correct endmembers with limited models. Meanwhile, their abundance maps are far away from others. The NMoG still
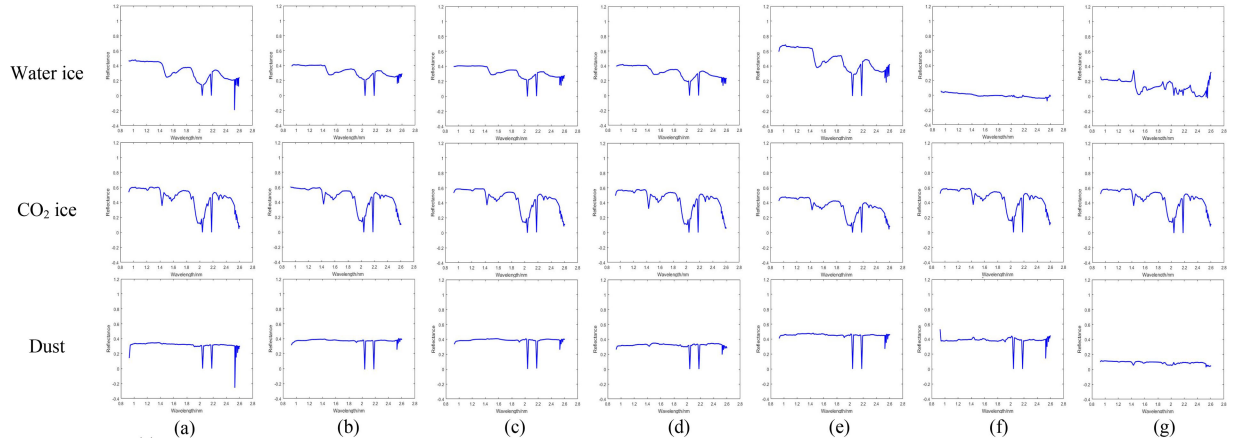
Fig. 18.   Extracted endmembers before and after denoising. (a) Original. (b) HSSNR. (c) BM4D. (d) LRTV. (e) NMoG. (f) ITSReg. (g) LLRT.
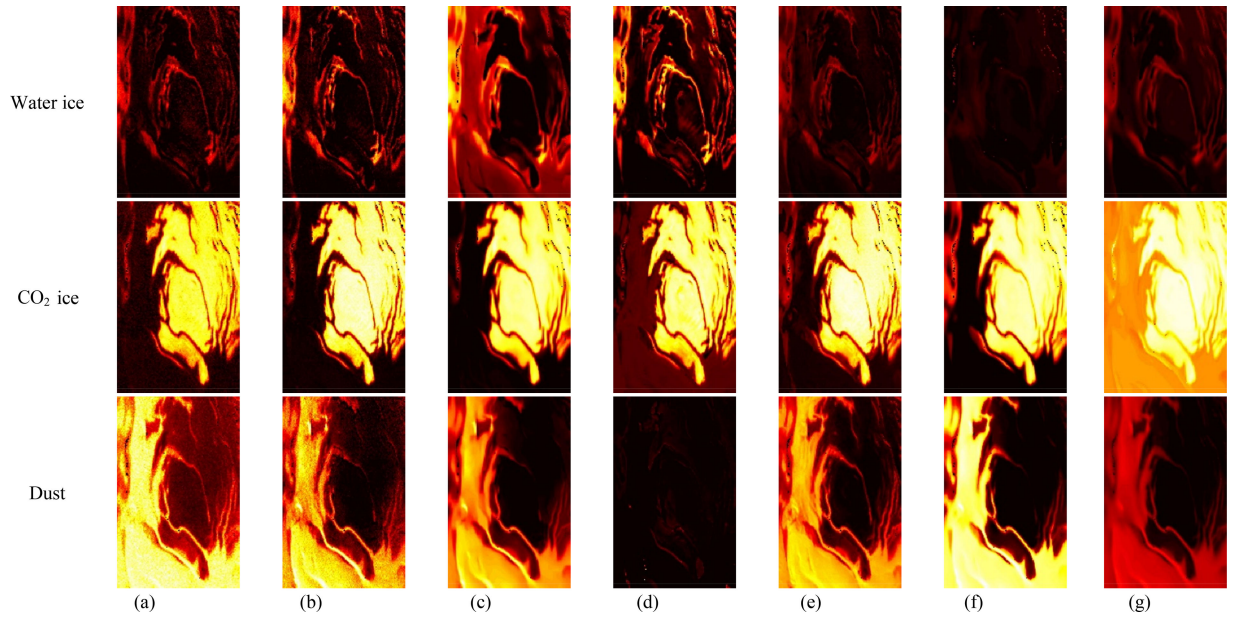

Fig. 19.   Abundance maps. (a) Original. (b) HSSNR. (c) BM4D. (d) LRTV. (e) NMoG. (f) ITSReg. (g) LLRT.

perform best. r values are higher than those of the reference spectra, and the spectral angle is also significantly reduced, but the dust distribution in LRTV has the greater error.

Black spots are observed at the same positions in each band of ORB0041. These spots correspond to the missing data as far as we are concerned. None of these algorithms can remove them. The same position in each band means the absence of redundant information for restoration. Their existence results in the poor performance of LRTV and tensor-based algorithms, because these modes do not consider non-i.i.d. degradation.

2) Discussion of Surface Materials' Spatial Distribution on the South Polar Permanent Cap: Bibring *et al.* [38] stated that perennial water ice was widely found on the south polar cap that acted as a small admixture to carbon dioxide in bright areas, and was being associated with dusts at the edges of bright CO_2-ice-rich cap. Abundance maps in Fig. 19 show that most of the denoising algorithms can maintain the spectral information

well, and the unmixing results are consistent with the known distribution.

The concentrations of CO_2 ice and dust distribute uniformly in the original results. However, the concentrations of the two components have changed after denoising. Furthermore, compared with the abundance maps before restoration, CO_2 ice concentration shows the highest value in the center of the bright region and decreases toward the periphery. The dust concentration gradually increased from the edge junction of the bright cap. The reasons for the concentration distribution change is speculated as the improved atmospheric correction and restored spectral information after denoising. As mentioned in Section V, joint spatial–spectral denoising can remove atmospheric effects and maintain the fidelity of spatial and spectral domains further, thereby reflecting a realistic surface distribution. Overall, we suppose that this gradual concentration distribution is close to the ground truth.

TABLE IV
COMPARISON OF QUANTITATIVE INDICATORS OF ENDMEMBERS' SPECTRAL SIGNATURE

Endmember	Correlation Coefficient				Spectral Angle		
	H_2O	CO_2	Dust		H_2O	CO_2	Dust
Original							
1	**0.8717**	0.7552	0.4272		**14.9533**	17.5113	19.0436
2	0.7649	**0.9177**	0.5888		14.3392	**12.1445**	16.0845
3	0.2481	0.3342	**0.3443**		13.1096	25.7988	**12.3086**
4	0.0308	-0.0102	0.3013		11.2019	28.6351	9.3459
5	0.0298	-0.0769	0.2897		15.7188	31.4555	13.7961
HSSNR							
1	**0.8448**	0.6973	0.5202		**8.2906**	20.1558	11.5681
2	0.7588	**0.9110**	0.5957		13.2183	**13.0629**	14.8543
3	0.7869	**0.9064**	0.5962		13.5009	**12.9136**	15.4110
4	0.5192	0.5931	0.3506		10.3156	22.2321	11.5876
5	0.1516	0.1364	**0.5110**		9.9546	27.2939	**7.3988**
BM4D							
1	**0.8312**	0.7270	0.5165		**8.4139**	19.6327	11.5604
2	0.7762	**0.9159**	0.7270		13.3392	**12.7080**	15.1435
3	0.0721	0.1240	**0.4862**		10.2156	27.3522	**7.4222**
4	-0.0915	0.0399	0.0131		18.4822	30.9173	17.6387
5	-0.3489	-0.5195	-0.0223		27.3079	44.2675	24.9768
LRTV							
1	**0.8566**	0.7990	0.5317		**9.3070**	17.6719	12.5922
2	0.2904	0.0005	0.2167		10.8780	29.0914	11.2286
3	0.7399	**0.9152**	0.5974		14.4475	**12.3191**	15.8768
4	0.7663	0.9149	0.5962		13.5576	12.6793	15.2608
5	0.1084	0.2773	**0.5477**		10.3454	26.1666	**7.2328**
NMoG							
1	**0.8746**	0.7146	0.4399		**11.1122**	18.9934	15.2678
2	0.8188	**0.9185**	0.5752		14.0764	**11.9676**	16.4728
3	0.7528	**0.9088**	0.6030		**13.0412**	13.2814	14.5573
4	0.1721	0.2019	0.4858		9.7928	26.7715	7.5498
5	-0.0031	-0.0589	0.3343		11.0092	28.8667	8.7836
ITSReg							
1	**0.7307**	0.5981	0.0408		90.0000	86.9134	90.0000
2	0.7615	**0.9073**	0.6030		**12.6893**	13.4910	14.2942
3	0.3238	0.3256	**0.5310**		8.9440	24.7651	**7.3002**
4	0.1654	-0.2787	-0.0998		22.2461	39.3315	24.0010
5	-0.8759	-0.7384	-0.2213		90.0000	90.0000	90.0000
LLRT							
1	**0.5395**	0.1038	0.0160		**28.7478**	39.9586	32.7222
2	0.6213	**0.9137**	0.3130		**9.5834**	16.8130	12.0586
3	0.7614	**0.9098**	0.6013		13.1883	**13.1068**	14.8029
4	-0.5102	-0.5640	-0.0206		19.3402	37.2949	16.2088
5	-0.0986	-0.2787	-0.2290		22.3624	38.0036	23.0469

VIII. CONCLUSION

In this work, we classified the noises on the planetary HSI in detail and tested the transferability of the current state-of-the-art terrestrial joint spatial–spectral denoising algorithms for planetary HSI datasets. In real experiments, the denoising results are evaluated quantitatively by applying the proposed method using HiRISE image. Furthermore, the unmixing results after noise removal are used to analyze the spectral fidelity and the spatial distribution representation ability of these HSI denoising methods further.

Experiments have proven that when spatial and spectral priors are considered, the regularization models can be transferred greatly to planetary HSI datasets and achieve the best denoising results, especially for the NMoG model, which considers the nonrandomly distributed noises. In practice, noises on real HSIs are usually non-i.i.d. Thus, such models can remove multiple types of noises effectively and be adopted to various planetary sensors. For tensor-based algorithms, HSIs are treated as three-order tensors to maintain the original structure, especially in the spatial domain, thereby restoring additional spatial details. However, they are often time-consuming due to the heavy computation burden when lacking effective enough optimization ways. Meanwhile, their modeling for mixed noises needs to be strengthened before transferring to planetary HSIs. Filter-based methods exhibit remarkable spectral fidelity albeit the visual results are not sufficient. Hence, filter-based models can be applied to planetary datasets with relatively slight degradation. Overall, approaches that model the non-i.i.d. noises can achieve remarkable performance on planetary HSIs. The experimental analysis in Russell Dunes and the south polar permanent cap infers that the joint spatial–spectral-based restoration methodologies may facilitate the atmospheric correction and maintain the information in two domains, thereby resulting in a realistic planetary surface distribution.

However, the experiment on OMEGA images reveals that these methods have not removed dead pixels that exists at

the same position of each band. The reason is that the redundant information to complete these black spots is lacking. The existence of missing data will affect the analysis of the spatial distribution [39] and the spatial–temporal variation characteristics of minerals greatly and would cause finding future landing sites. Therefore, future research efforts are directed toward designing novel algorithms that can repair missing information while denoising.

ACKNOWLEDGMENT

REFERENCES

[1] J. F. Mustard, "From planets to crops and back: Remote sensing makes sense: Planetary remote sensing," *J. Geophys. Res.*, vol. 122, no. 4, pp. 794–797, Apr. 2017.

[2] C. M. Pieters *et al.*, "Character and spatial distribution of oh/h$_2$o on the surface of the moon seen by M³ on chandrayaan-1," *Science*, vol. 326, no. 5952, pp. 568–572, Oct. 2009.

[3] J.-P. Bibring *et al.*, "OMEGA: Observatoire pour la Minéralogie, l'Eau, les Glaces et l'Activité," in *Proc. Mars Express, Sci. Payload*, 2004, pp. 37–49.

[4] S. Murchie *et al.*, "Compact reconnaissance imaging spectrometer for mars (CRISM) on mars reconnaissance orbiter (MRO)," *J. Geophys. Res. Planets.*, vol. 112, no. E5, pp. 431–433, May 2007.

[5] Q. Xie *et al.*, "Multispectral images denoising by intrinsic tensor sparsity regularization," in *Proc. IEEE Comput. Soc. Conf. Comput. Vis. Pattern Recognit.*, Jun. 2016, pp. 1692–1700.

[6] Q. Yuan, Z. Qiang, L. Jie, S. Huanfeng, and Z. Liangpei, "Hyperspectral image denoising employing a spatial-spectral deep residual convolutional neural network," *IEEE Trans. Geosci. Remote Sens.*, vol. 57, no. 2, pp. 1–14, Feb. 2019.

[7] H. Othman and S.-E. Qian, "Noise reduction of hyperspectral imagery using hybrid spatial-spectral derivative-domain wavelet shrinkage," *IEEE Trans. Geosci. Remote Sens.*, vol. 44, no. 2, pp. 397–408, Jan. 2006.

[8] M. Maggioni, V. Katkovnik, K. Egiazarian, and A. Foi, "Nonlocal transform-domain filter for volumetric data denoising and reconstruction," *IEEE Trans. Image Process.*, vol. 22, no. 1, pp. 119–133, Jul. 2012.

[9] Q. Shi *et al.*, "Domain adaption for fine-grained urban village extraction from satellite images," *IEEE Geosci. Remote Sens. Lett.*, vol. 17, no. 8, pp. 1430–1434, Aug. 2020.

[10] L. I. Rudin, S. Osher, and E. Fatemi, "Nonlinear total variation based noise removal algorithms," *Physica D*, vol. 60, no. 1–4, pp. 259–268, Nov. 1992.

[11] T. Gan and W. Lu, "Image denoising using multi-stage sparse representations," in *Proc. IEEE Int. Conf. Image Process.*, Sep. 2010, pp. 1165–1168.

[12] H. Zhang, W. He, L. Zhang, H. Shen, and Q. Yuan, "Hyperspectral image restoration using low-rank matrix recovery," *IEEE Trans. Geosci. Remote Sens.*, vol. 52, no. 8, pp. 4729–4743, Oct. 2013.

[13] Q. Shi, B. Du, and L. Zhang, "Domain adaptation for remote sensing image classification: A low-rank reconstruction and instance weighting label propagation inspired algorithm," *IEEE Trans. Geosci. Remote Sens.*, vol. 53, no. 10, pp. 5677–5689, May 2015.

[14] W. He, H. Zhang, L. Zhang, and H. Shen, "Total-variation-regularized low-rank matrix factorization for hyperspectral image restoration," *IEEE Trans. Geosci. Remote Sens.*, vol. 54, no. 1, pp. 178–188, Jul. 2015.

[15] Y. Chen, X. Cao, Q. Zhao, D. Meng, and Z. Xu, "Denoising hyperspectral image with non-i.i.d. noise structure," *IEEE Trans. Cybern.*, vol. 48, no. 3, pp. 1054–1066, Mar. 2018.

[16] Y. Chang, L. Yan, and S. Zhong, "Hyper-laplacian regularized unidirectional low-rank tensor recovery for multispectral image denoising," in *Proc. IEEE Comput. Soc. Conf. Comput. Vis. Pattern Recognit.*, Jul. 2017, pp. 4260–4268.

[17] H. Liu, N. Klomp, and I. Heynderickx, "A no-reference metric for perceived ringing artifacts in images," *IEEE Trans. Circuits Syst. Video Technol.*, vol. 20, no. 4, pp. 529–539, Apr. 2010.

[18] M. Parente, B. L. Ehlmann, A. M. Saranathan, S. Wiseman, and L. Pan, "Denoising CRISM images: A new look," in *Proc. Lunar Planet. Sci. Conf.*, Mar. 2014, Paper 2900.

[19] F. Morgan, F. Seelos, and S. Murchie, "CRISM data users' workshop cat tutorial," 2019. [Online] Available: http://pds-geosciences.wustl.edu/work shops

[20] K. Stamnes, S.-C. Tsay, W. Wiscombe, and K. Jayaweera, "Numerically stable algorithm for discrete- ordinate- method radiative transfer in multiple scattering and emitting layered media," *Appl. Opt.*, vol. 27, no. 12, pp. 2502–2509, Jun. 1988.

[21] J. Bell *et al.*, "Mineralogic and compositional properties of martian soil and dust: Results from mars pathfinder," *J. Geophys. Res. Planets.*, vol. 105, no. E1, pp. 1721–1755, Jan. 2000.

[22] S. Nakhostin, H. Clenet, T. Corpetti, and N. Courty, "Joint anomaly detection and spectral unmixing for planetary hyperspectral images," *IEEE Trans. Geosci. Remote Sens.*, vol. 54, no. 12, pp. 6879–6894, Dec. 2016.

[23] J. Liu, B. Luo, S. Douté, and J. Chanussot, "Exploration of planetary hyperspectral images with unsupervised spectral unmixing: A case study of planet Mars," *Remote Sens.*, vol. 10, no. 5, May 2018, Art. no. 737.

[24] J. Wright, A. Ganesh, S. Rao, Y. Peng, and Y. Ma, "Robust principal component analysis: Exact recovery of corrupted low-rank matrices via convex optimization," in *Proc. NIPS*, 2009, pp. 2080–2088.

[25] A. S. McEwen, C. Hansen-Koharcheck, and A. Espinoza, *Mars: The Pristine Beauty of the Red Planet*. Tucson, AZ, USA: Univ. Arizona Press, 2017.

[26] L. Miao and H. Qi, "Endmember extraction from highly mixed data using minimum volume constrained nonnegative matrix factorization," *IEEE Trans. Geosci. Remote Sens.*, vol. 45, no. 3, pp. 765–777, Mar. 2007.

[27] X. Ceamanos, S. Douté, B. Luo, F. Schmidt, G. Jouannic, and J. Chanussot, "Intercomparison and validation of techniques for spectral unmixing of hyperspectral images: A planetary case study," *IEEE Trans. Geosci. Remote Sens.*, vol. 49, no. 11, pp. 4341–4358, Nov. 2011.

[28] A. S. McEwen *et al.*, "Mars reconnaissance orbiter's high resolution imaging science experiment (HiRISE)," *J. Geophys. Res. Planets.*, vol. 112, no. E5, p. E05S02, May 2007.

[29] Z. Bian and X. Zhang, *Pattern Recognition*. Tsinghua, China: Univ. Press, 2000.

[30] Q.-S. Chen, M. Defrise, and F. Deconinck, "Symmetric phase-only matched filtering of Fourier-Mellin transforms for image registration and recognition," *IEEE Trans. Pattern Anal. Mach. Intell.*, no. 12, pp. 1156–1168, Dec. 1994.

[31] C. G. Harris and M. Stephens, "A combined corner and edge detector," in *Proc. 4th Alvey Vis. Conf.*, Sep. 1988, pp. 147–151.

[32] M. A. Fischler and R. C. Bolles, "Random sample consensus: A paradigm for model fitting with applications to image analysis and automated cartography," *Commun. ACM*, vol. 24, no. 6, pp. 381–395, Jun. 1981.

[33] E. Gardin, P. Allemand, C. Quantin, and P. Thollot, "Defrosting, dark flow features, and dune activity on Mars: Example in Russell crater," *J. Geophys. Res. Planets.*, vol. 115, no. E6, p. E06016, Jun. 2010.

[34] J. Eluszkiewicz, J.-L. Moncet, T. N. Titus, and G. B. Hansen, "A microphysically-based approach to modeling emissivity and albedo of the martian seasonal caps," *Icarus*, vol. 174, no. 2, pp. 524–534, Apr. 2005.

[35] A. S. Hale, D. Bass, and L. Tamppari, "Monitoring the perennial martian northern polar cap with MGS MOC," *ICARUS*, vol. 174, no. 2, pp. 502–512, Apr. 2005.

[36] S. Douté *et al.*, "South pole of mars: Nature and composition of the icy terrains from mars express OMEGA observations," *Planet. Space Sci.*, vol. 55, no. 1, pp. 113–133, Jan. 2007.

[37] P. R. Christensen *et al.*, "Mars global surveyor thermal emission spectrometer experiment: Investigation description and surface science results," *J. Geophys. Res. Planets.*, vol. 106, no. E10, pp. 23823–23871, Oct. 2001.

[38] J.-P. Bibring, "Perennial water ice identified in the south polar cap of Mars," *Nature*, vol. 428, no. 6983, Apr. 2004, Art. no. 627.

[39] Q. Zhang, Q. Yuan, C. Zeng, X. Li, and Y. Wei, "Missing data reconstruction in remote sensing image with a unified spatial-temporal-spectral deep convolutional neural network," *IEEE Trans. Geosci. Remote Sens.*, vol. 56, no. 8, pp. 4274–4288, Aug. 2018.

[40] C. R. Webster, P. R. Mahaffy, S. K. Atreya, G. J. Flesch, and K. A. Farley, "Low upper limit to methane abundance on mars," *Science*, vol. 342, no. 6156, pp. 355–357, Oct. 2003.

Shuheng Zhao received the B.S. degree in geodesy and geomatics engineering from the Wuhan University, Wuhan, China, in 2018. She is currently working toward the M.S. from the in State Key Laboratory of Information Engineering at Surveying, Mapping, and Remote Sensing (LIESMARS), Wuhan University, Wuhan, China.

Her research interests include planetary remote sensing and hyperspectral image processing.

Jie Li (Member, IEEE) received the B.S. degree in sciences and techniques of remote sensing and the Ph.D. degree in photogrammetry and remote sensing from Wuhan University, Wuhan, China, in 2011 and 2016, respectively.

He is currently an Associate Professor with the School of Geodesy and Geomatics, Wuhan University. His research interests include image quality improvement, image super-resolution reconstruction, data fusion, remote sensing image processing, sparse representation, and deep learning.

Qiangqiang Yuan (Member, IEEE) received the B.S. degree in surveying and mapping engineering and the Ph.D. degree in photogrammetry and remote sensing from Wuhan University, Wuhan, China, in 2006 and 2012, respectively.

In 2012, he joined the School of Geodesy and Geomatics, Wuhan University, where he is currently a Professor. He has authored or coauthored more than 70 research papers, including more than 60 peer-reviewed articles in international journals such as the IEEE TRANSACTIONS IMAGE PROCESSING and the IEEE TRANSACTIONS ON GEOSCIENCE AND REMOTE SENSING. His current research interests include image reconstruction, remote sensing image processing and application, and data fusion.

Dr. Yuan was the recipient of the Youth Talent Support Program of China in 2019, and the Top-Ten Academic Star of Wuhan University, in 2011. In 2014, he received the Hong Kong Scholar Award from the Society of Hong Kong Scholars and the China National Postdoctoral Council. He is an Associate Editor of IEEE ACCESS journal, and has frequently served as a Referee for more than 40 international journals for remote sensing and image processing.

Huanfeng Shen (Senior Member, IEEE) received the B.S. degree in surveying and mapping engineering and the Ph.D. degree in photogrammetry and remote sensing from Wuhan University, Wuhan, China, in 2002 and 2007, respectively.

In 2007, he joined the School of Resource and Environmental Sciences (SRES), Wuhan University, where he is currently a Luojia Distinguished Professor and Associate Dean of SRES. He was or is the PI of two projects supported by the National Key Research and Development Program of China, and six projects supported by National Natural Science Foundation of China. He has authored more than 100 research papers in peer-reviewed international journals. His research interests include remote sensing image processing, multisource data fusion, and intelligent environmental sensing.

He is a Senior Member of Council Member of China Association of Remote Sensing Application, Education Committee Member of Chinese Society for Geodesy Photogrammetry and Cartography, and Theory Committee Member of Chinese Society for Geospatial Information Society. He is currently a member of the Editorial Board of *Journal of Applied Remote Sensing and Geography and Geo-Information Science*.

Liangpei Zhang (Fellow, IEEE) received the B.S. degree in physics from Hunan Normal University, Changsha, China, in 1982, the M.S. degree in optics from the Xi'an Institute of Optics and Precision Mechanics, Chinese Academy of Sciences, Xi'an, China, in 1988, and the Ph.D. degree in photogrammetry and remote sensing from Wuhan University, Wuhan, China, in 1998.

He is a Chair Professor with State Key Laboratory of Information Engineering, Surveying, Mapping, and Remote Sensing (LIESMARS), Wuhan University. He was a Principal Scientist for the China State Key Basic Research Project (2011–2016) appointed by the Ministry of National Science and Technology of China to lead the remote sensing program in China. He has authored or coauthored more than 700 research papers and five books. He is the Institute for Scientific Information (ISI) highly cited author. He is the holder of 30 patents. His research interests include hyperspectral remote sensing, high-resolution remote sensing, image processing, and artificial intelligence.

Dr. Zhang is a Fellow of Institution of Engineering and Technology (IET). He was the recipient of the 2010 best paper Boeing award, the 2013 best paper ERDAS award from the American Society of Photogrammetry and Remote Sensing (ASPRS) and 2016 best paper theoretical innovation award from the International Society for Optics and Photonics (SPIE). His research teams won the top three prizes of the IEEE GRSS 2014 Data Fusion Contest, and his students have been selected as the winners or finalists of the IEEE International Geoscience and Remote Sensing Symposium (IGARSS) student paper contest in recent years. He also serves as an Associate Editor or Editor of more than ten international journals. He is currently serving as an Associate Editor of the IEEE TRANSACTIONS ON GEOSCIENCE AND REMOTE SENSING. He is the founding Chair of IEEE Geoscience and Remote Sensing Society (GRSS) Wuhan Chapter.